Interfacial solvation-structure regulation for stable Li metal anode by a desolvation coating technique

3 4 5 6	Guo-Xing Li ^a , Peter Lennartz ^b , Volodymyr Koverga ^{c,d} , Rong Kou ^a , Au Nguyen ^e , Heng Jiang ^a , Meng Liao ^a , Daiwei Wang ^a , Naveen Dandu ^{c,d} , Michael Zepeda ^c , Haiying Wang ^f , Ke Wang ^f , Anh T. Ngo ^{c,d,1} , Gunther Brunklaus ^{b,1} and Donghai Wang ^{a,1}
7	Author affiliations:
8	^a Department of Mechanical Engineering, The Pennsylvania State University, University Park, PA16802, United States.
9	^b Forschungszentrum Jülich GmbH, Helmholtz Institute Münster, IEK-12, Münster 48149, Germany.
10	^c Department of Chemical Engineering, University of Illinois Chicago, Chicago, IL 60608, United States.
11	^d Materials Science Division, Argonne National Laboratory, Lemont, IL 60439, United States.
12	^e Department of Materials Science and Engineering, The Pennsylvania State University, University Park, PA 16802, United States.
13	Materials Research Institute, The Pennsylvania State University, University Park, PA 16802, United States.
14	¹ To whom correspondence may be addressed. Email: anhngo@uic.edu, g.brunklaus@fz-juelich.de, dwang@psu.edu.
15	Classification: Physical Science/Engineering.
16 17 18 19 20	Author contributions: GX. L. and Do. W. conceived and designed the idea. GX. L., R. K. and H. J. conducted the electrochemical tests, ¹ H, ¹² and ¹⁹ F NMR characterization. P. L. and G. B. performed and analyzed the operando ⁷ Li NMR studies. V. K., N. D. and M. Z performed M simulations and DFT calculations. A. T. N. supervised the molecular modelling. A. N., M. L. and Da. W. conducted and analyzed the XPS dep profiling characterization. H. W. and K. W. conducted the cryo-TEM experiments. GX. L., A. T. N., G. B. and Do. W. wrote and revised the paper.
21	The authors declare no competing interests.
22	
23	
24	
25	
26	
27	
28	
29	
30	
31	

Rechargeable lithium (Li) metal batteries face challenges in achieving stable cycling due to the instability of the solid electrolyte interphase (SEI). The Li-ion solvation structure and its desolvation process are crucial for the formation of a stable SEI on Li metal anodes and improving Li plating/stripping kinetics. This research introduces an interfacial desolvation coating technique to actively modulate the Li-ion solvation structure at the Li metal interface and regulate the participation of the electrolyte solvent in SEI formation. Through experimental investigations conducted using a carbonate electrolyte with limited compatibility to Li metal, the optimized desolvation coating layer, composed of 12-crown-4 ether-modified silica materials, selectively displaces strongly coordinating solvents while simultaneously enriching weakly coordinating fluorinated solvents at the Li metal/electrolyte interface. This selective desolvation and enrichment effect reduce solvent participation to SEI and thus facilitate the formation of a LiF-dominant SEI with greatly reduced organic species on the Li metal surface, as conclusively verified through various characterization techniques including XPS, quantitative NMR, operando NMR, cryo-TEM, EELS, and EDS. The interfacial desolvation coating technique enables excellent rate cycling stability (i.e., 1C) of the Li metal anode and prolonged cycling life of the Li||LiCoO₂ pouch cell in conventional carbonate electrolyte (E/C 2.6 g/Ah), with 80% capacity retention after 333 cycles.

lithium metal anode | solid electrolyte interphase | selective desolvation coating

Significance

Forming a stable solid electrolyte interphase (SEI) on Li metal anodes is challenging while pivotal to enable rechargeable lithium (Li) metal batteries with high-energy-density and long cycle life. Addressing this challenge, this research presents an interfacial desolvation coating technique that actively modulates the Li-ion solvation structure at the Li metal interface. By selectively displacing strongly coordinating solvents and enriching weakly coordinating fluorinated solvents, the optimized desolvation coating layer promotes the formation of a LiF-dominant SEI on the Li metal surface. This desolvation technique significantly reduces solvent participation in SEI formation, leading to substantially enhanced stability of Li metal anode even in the challenging conventional carbonate electrolyte.

33

34

35

36

37

38

39 40

41

42

43

44

45

46

47

48

49

50

51

52

53

54

55

56

57 58

59 60

Rechargeable Li metal batteries are one of the most promising next-generation high-energydensity battery technologies (1). However, the stable cycling of Li metal anodes has long been hindered by uncontrollable Li dendrite formation and low Coulombic efficiency (CE) due to the repeated breakdown/reformation of SEI layer derived from electrolyte decomposition on the Li metal anode surface (2, 3). The intrinsic process of SEI formation involves solvated Li-ion transport through an electric double layer, its desolvation at the inner Helmholtz plane, followed by Li-ion reduction and the desolvated solvent reduction on Li metal. The composition and structure of SEI contributed by electrolyte decomposition are affected by the composition of the electrolyte, including Li salts, solvents, additives, and the solvation structure of Li-ion. So far, considerable strategies have been explored to generate a robust SEI for Li metal anode, including tuning electrolyte composition (4–10), engineering interfacial properties (11–14), and applying a protective layer to block/mitigate electrolyte decomposition during SEI formation (15–17). The developed strategies validate that the formation of an electrochemically and mechanically stable SEI layer can improve the cycling life of Li metal anodes by regulating the formation of SEI layers with components such as LiF (18) and Li₂O (19), and by controlling their nanoscale spatial distribution, such as mosaic, layered, or monolithic structures, within the SEI layer (20, 21). However, as the SEI may still experience cracking and damage upon Li plating/striping, the electrolyte will inevitably contact Li metal to participate SEI reformation process, and thus the electrolyte-derived SEI still plays an essential role in sustaining the (re)formed SEI layer to enable stable Li metal cycling (22, 23).

64

65

66

67

68

69

70

71

72

73

74

75

76

77

78

79

80

81

82

83

84

85

86

The liquid electrolyte-directed SEI comprises the inorganic and organic components with its composition and structures governed by the intrinsic solvation of Li-ion with organic electrolyte solvents and by the reactivities of anions and solvents with Li metal anodes (24). The recent

development of SEI chemistry and engineering typically employed fluorinated co-solvent and/or fluorine-containing Li salts to enhance the generation of inorganic component in SEI with controlled nanostructures (25, 26). While, it is still challenging to regulate the involvement of organic solvent in the SEI formation process since Li-ion coordinating organic solvent inevitably participate the SEI formation and often randomly contributes to form the organic component during the SEI formation (27). Thus far, the actual fine-tuning of Li-ion solvation structure at the Li metal/electrolyte interface, tailoring of organic solvent participation in the SEI formation process, and control of SEI functionality on Li metal anodes are particularly important.

87

88

89

90

91

92

93

94

95

96

97

98

99

100

101

102

103

104

105

106

107

108

109

Herein, we demonstrate a strategy of desolvation coating technique to alter the Li-ion solvation structure at the Li metal/electrolyte interface, tune the electrolyte solvent contribution to SEI formation, and thus control the composition and nanostructure of the self-formed SEI layer. In this coating layer schematically illustrated in Fig. 1, the strongly Li-ion coordinating solvent is selectively displaced to the bulk electrolyte, and simultaneously the weakly Li-ion coordinating fluorinated solvent increasingly involves Li-ion solvation, resulting in suppressed electrolyte solvent participation in SEI formation process and a stable LiF-dominant SEI layer with greatly reduced organic species. We first explore various functional molecules of linear ether, branched amine, and crown ether to study their effects on Li-ion solvation structures by ¹³C nuclear magnetic resonance (NMR) techniques, and density functional theory (DFT) calculations and molecular dynamics (MD) simulations. The 12-crown-4 ether (12-C-4) was identified to show a strong effect on changing the solvation structure of Li-ion. The desolvation coating layer is therefore fabricated using surface-functionalized silica materials covalently modified with 12-C-4 or linear ether. As a proof of concept, we applied a desolvation coating layer on Li metal in conventional carbonate electrolyte to mitigate the pronounced reactivity between carbonate

electrolytes and the Li metal anode, thus addressing the significant challenges associated with the utilization of these electrolytes in Li metal batteries. The 12-C-4 ether functionalized silica (CES) coating layer demonstrates a desolvation selectivity on strongly coordinating electrolyte solvent ethylene carbonate (EC) over weakly coordinating solvents such as diethyl carbonate (DEC) and fluoroethylene carbonate (FEC), in contrast to negligible desolvation effect observed from the liner polyethylene oxide functionalized silica (PEOS) coating layer. In addition, the desolvation coating layer CES also enables increased participation of FEC, a weakly coordinating solvent that has the capability of generating LiF and is typically used as an SEI forming agent (28), in Li-ion solvation. As a result, the introduced CES alters the Li-ion solvation structure at the Li/electrolyte interface, reduces the solvent contribution to the SEI formation and facilitates an inorganic-rich SEI with LiF as the dominant species, as verified by high-resolution and depthprofiling X-ray photoelectron spectroscopy (XPS) analysis and cryogenic transmission electron microscopy (cryo-TEM). The use of CES coating layer with the selective desolvation functionality boosts Li plating/striping CE to 99.1% in conventional carbonate electrolyte, delivers improved rate performance of Li metal anodes, and enables a remarkable cycling life of a Li||LiCoO₂ (LCO) pouch cell with an 80% capacity retention after 333 cycles under practical conditions (LCO 3.3 mAh/cm², negative/positive electrode capacity (N/P) ratio of 3.0 and electrolyte/capacity (E/C) ratio of 2.6 g/Ah). The selective desolvation coating layer effectively retards the electrolyte decomposition verified by quantitative ¹⁹F and ¹H NMR technique and unveils the solution to the conundrum of incompatibility between Li metal anodes and electrolytes.

110

111

112

113

114

115

116

117

118

119

120

121

122

123

124

125

126

127

128

129

Selective displacement of strongly Li-ion coordinating solvent & enrichment of SEI forming agent of interfacial Li-ion solvation by a desolvation coating layer

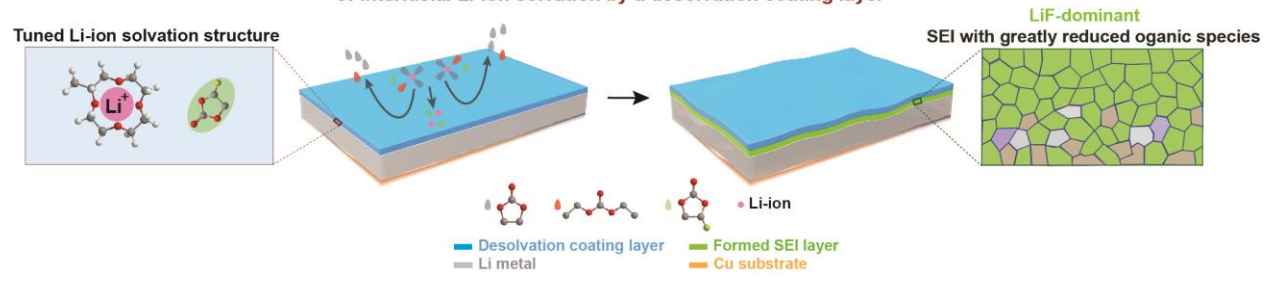


Fig. 1. Schematic illustrations of the interfacial Li-ion solvation structure tuned by a selective desolvation coating technique. The solvation structure of Li-ion can be tuned and selectively desolvated by the 12-C-4 ether installed coating layer. The developed selective desolvation technique facilitates a stable inorganic-rich SEI with LiF as the dominant species and greatly reduced organic species.

Results and discussions

Starting from functional molecules with strong Li-ion coordinating capability for Li-ion enrichment effects (29, 30), we investigate the branched amine (polyethylenimine, PEI), linear ether (polyethylene oxide, PEO), and crown ether 12-C-4 to reveal their potential in altering Li-ion solvation structure. The PEI, PEO, and 12-C-4 with an equivalent mole of coordination sites (N or O) were added separately to the single-solvent electrolyte of 1M LiPF₆ in DEC. The resulting electrolytes were analyzed by using ¹³C NMR technique (*SI Appendix*, Fig. S1). Interestingly, only in the presence of 12-C-4, the carbonyl carbon of DEC showed a noticeable upfield chemical shift (0.24 ppm), suggesting an increase of free DEC molecules and change of Li-ion solvation structure by the addition of 12-C-4, attributed to the specific selectivity/coordination ability of 12-C-4 to Li-ion (31).

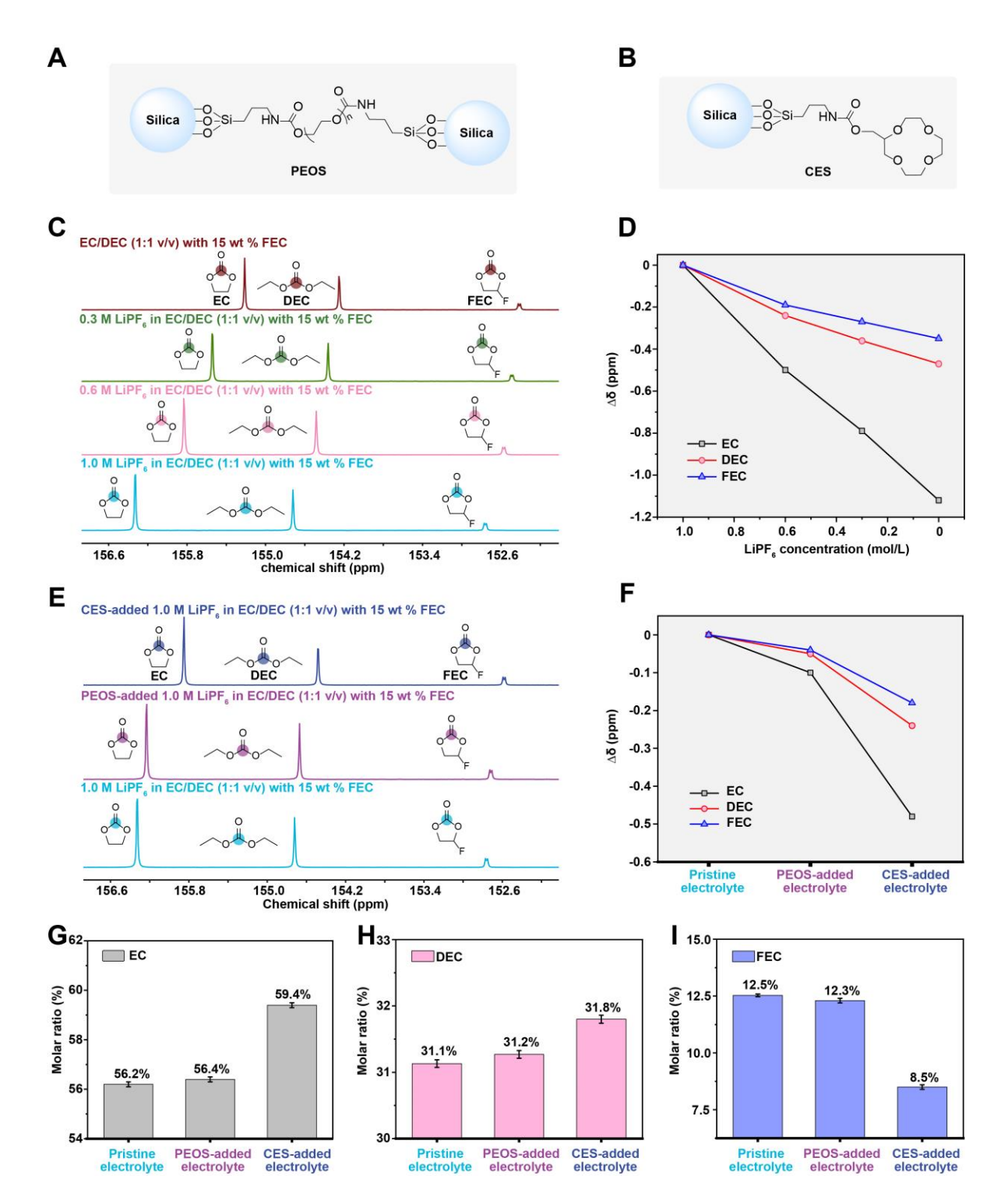


Fig. 2. Chemical structures of PEOS, CES and the NMR spectroscopic analysis of electrolytes. (**A**) The chemical structure of POES. (**B**) The chemical structure of CES. (**C**) The ¹³C NMR spectra of electrolytes with different concentrations of LiPF₆ in EC/DEC (1:1 v/v) with 15 wt% FEC. (**D**) The plots of chemical shift differences of the EC, DEC and FEC carbonyl carbons with different LiPF₆ concentrations. (**E**) The ¹³C NMR spectra of pristine mixed carbonate electrolyte, PEOS-added and CES-added electrolytes. (**F**) The plots of chemical shift differences of the EC, DEC and FEC carbonyl carbons in the pristine electrolyte, PEOS-added and CES-added electrolyte. (**G**–**I**) The ¹H NMR determined molar ratios of EC, DEC and FEC of the pristine electrolyte (**G**), PEOS-added electrolyte (**H**) and CES-added electrolyte (**I**), the molar ratio values were obtained by averaging the results from 3 parallel experiments.

To realize interfacial manipulation of Li-ion desolvation for SEI formation, the 12-C-4 ether were covalently installed onto the silica nanoparticles surface, followed by coating on top of the Li metal anode to serve as a desolvation coating layer. The coating layer is designed to promote the Li-ion desolvation at the interface of Li metal, aiming to facilitate an inorganic-rich robust SEI formation by mitigating the parasitic reactions between organic electrolyte solvent and Li metal anode. A PEOS coating layer containing linear PEO functional groups with mainly Li-ion enrichment effects and negligible desolvation effect was also synthesized as a control and evaluated to prove the superiority of the CES coating layer (*SI Appendix*, Scheme S1–3).

157

158

159

160

161

162

163

164

165

166

167

168

169

170

171

172

173

174

175

176

177

178

179

With PEOS and CES materials in hand, we investigate the Li-ion solvation in a conventional mixed carbonate electrolyte (1 M LiPF₆ in EC/DEC (v/v = 1:1) with 15 wt % FEC) using 13 C NMR analysis. First, as shown in Fig. 2C, the electrolytes with different concentrations of LiPF₆ were studied by the ¹³C NMR technique showing chemical shift differences of carbonate solvents of EC, DEC and FEC. The ¹³C chemical shifts of the carbonyl carbons of EC, DEC, and FEC all gradually move upfield as the concentrations of LiPF₆ decrease, reflecting the changes in the chemical environment for the carbonyl carbons of EC, DEC, and FEC due to the weaker solvation of carbonate solvents with Li-ion and more free carbonate solvents. Interestingly, the chemical shift difference between the specific LiPF₆ concentration and 1 M LiPF₆ among the carbonyl carbons increases orderly from FEC, DEC to EC (Fig. 2D), indicating the strongest coordination capability between EC and Li-ion while the weakest coordination capability of FEC with Li-ion. Next, when PEOS added into the electrolyte of 1 M LiPF₆ in EC/DEC (v/v = 1:1) with 15 wt% FEC, very slight upfield chemical shifts of the carbonyl carbons (< 0.1 ppm) in ¹³C NMR are observed. This result indicates that the PEOS with Li-ion coordination functionality negligibly influences the Li-ion solvation structure. In contrast,

noticeable upfield chemical shift differences, i.e., 0.48 ppm for EC, 0.24 ppm for DEC and 0.18 ppm for FEC, are observed when the CES is added to the electrolyte (Fig. 2*E* and 2*F*). The distinguished upfield chemical shifts of EC, DEC and FEC between PEOS-added and CES-added electrolytes indicate that the CES can not only effectively dissociate the solvation complexes of Li-ion with carbonate solvents (i.e., desolvation), but also demonstrate a preferential desolvation effect on the strong Li-ion-coordination solvent EC (higher upfield chemical shift of 0.48 ppm for EC than that for DEC and FEC) over the weakly coordinating solvents DEC and FEC in CES-added electrolyte. It is worth noting that the CES can also facilitate the desolvation effect of Li-ion in the ether-based electrolyte, such as the localized high-concentration electrolyte LiFSI-1.2DME-3TTE (molar ratio, DME: 1,2-dimethoxyethane, TTE: 1,1,2,2-tetrafluoroethyl-2,2,3,3-tetrafluoropropyl ether) (*SI Appendix*, Fig. S16).

To quantitatively verify the disclosed desolvation effect, the molar ratios of EC, DEC, and FEC in the CES-added or PEOS-added electrolyte and pristine mixed carbonate electrolyte were determined by ¹H quantitative NMR analysis (Fig. 2*G–I*). Compared to the pristine electrolyte, the CES-added electrolyte showed an increased EC molar ratio from 56.2% to 59.4%, a slightly increased DEC molar ratio from 31.1% to 31.8%, and a much-decreased FEC molar ratio from 12.5% to 8.5%. In contrast, the PEOS-added electrolyte showed a negligible difference in molar ratios of each solvent compared to the pristine electrolyte. These quantitative results revealed by ¹H NMR, suggest that the CES material enables the preferential displacement of EC into the bulk electrolyte solution, while demonstrating an enrichment of FEC within the CES material matrix. With the Li-ion solvation structure tuned by CES material, the contribution of the solvents EC and FEC to the SEI formation at the Li metal/electrolyte interface can be significantly altered.

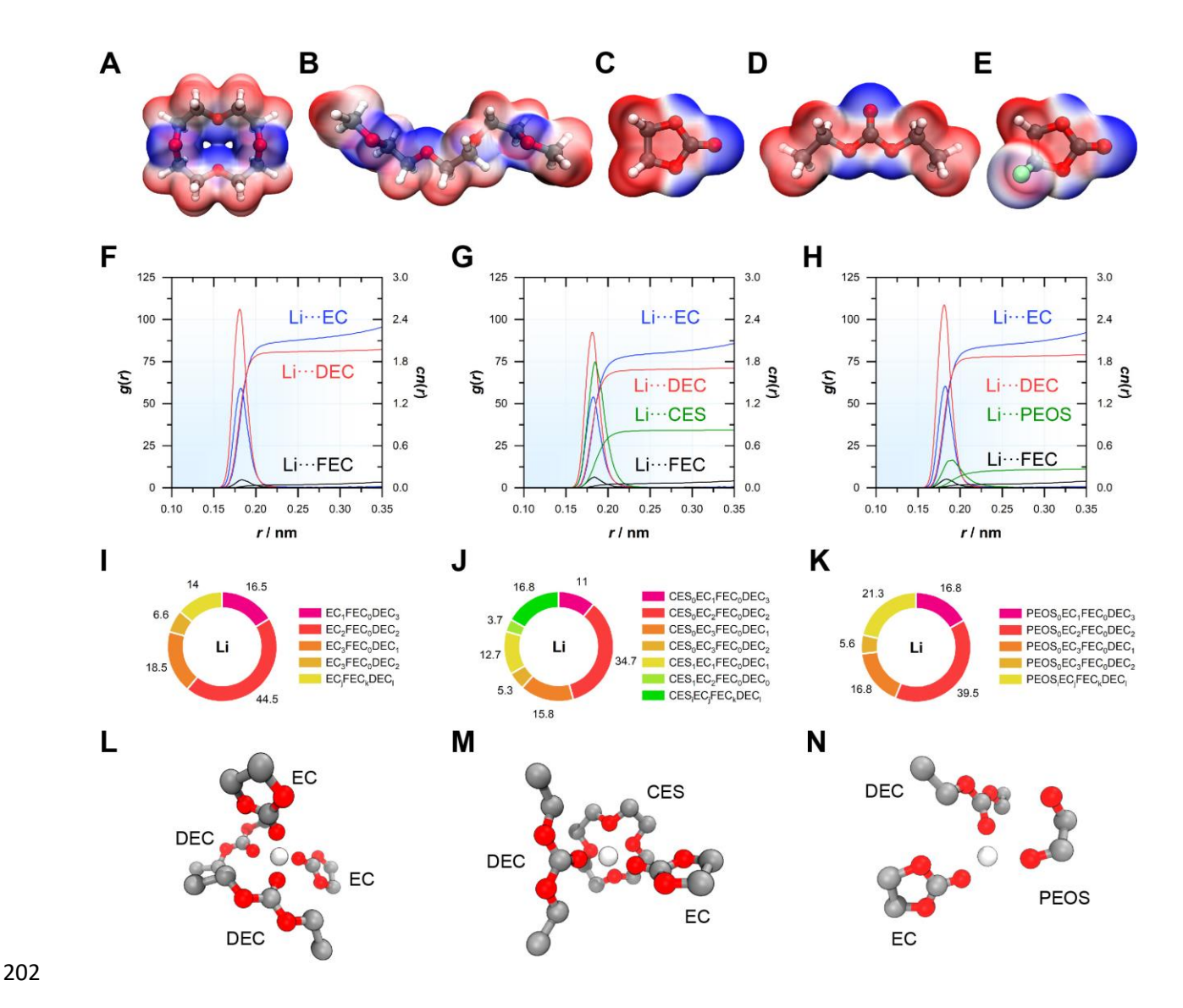


Fig. 3. DFT and MD studies of the Li-ion solvation structures. Electronic structure of 12-C-4 (**A**), triglyme (**B**), EC (**C**), DEC (**D**) and FEC (**E**) molecules included in electrolyte, represented by electrostatic potential map. Blue, white and red color correspond to electrostatic potential varying from minimum level of -78.76 kJ mol⁻¹ to maximum level of 78.76 kJ mol⁻¹. Li local environment and coordination ability represented in terms of the interactions with carbonyl oxygen atom of EC, DEC and FEC for neat pristine electrolyte (**F**), pristine electrolyte reached by 12-C-4 (**G**) and ethylendioxy (**H**) moieties, based on radial distribution function, g(r), and running coordination number, cn(r). Probability distribution (in %) of Li-molecular complexes in the first solvation shell of Li for neat pristine electrolyte (**I**), pristine electrolyte reached by 12-C-4 (**J**) and ethylendioxy (**K**) moieties, where Li-molecular complexes with probability < 3.5% are merged and represented as a combined contribution LiCES₁EC₁FEC_kDEC₁ and LiPEOS₁EC₁FEC_kDEC₁ for clarity (see also *SI Appendix*, Fig. S22). Illustration of the ensemble averaged Li-ion solvation structure for neat pristine electrolyte (**L**), pristine electrolyte reached by 12-C-4 (**M**) and triglyme (**N**) moieties.

The DFT calculations were further employed to support the NMR measurements on the Li-ion solvation structure. The preliminary analysis of the electronic structure of the electrolyte

constituents shows a high electron density at the vicinity of ether oxygen for 12-C-4 and triglyme, representing CES and PEOS, respectively (Fig. 3*A*–*B*), whereas the EC, DEC and FEC featured by a relatively higher electron density on carbonyl oxygen (Fig. 3*C*–*E*). Introducing Li⁺ to PEOS results in the formation of two energetically favorable configurations with open-chain and curled structures, similar to those obtained for Li⁺/CES complexes (*SI Appendix*, Fig. S21). The addition of solvent molecules to the Li⁺/CES and Li⁺/PEOS complexes does not alter the PEOS and CES structure and also demonstrates a higher binding energy for EC compared to FEC and DEC. On the other hand, for all the considered ion-molecular complexes, a higher binding energy was found for curled PEOS structures, which seemingly contradicts the CES desolvation ability. To gain further insight into the Li solvation structure, MD simulations of the condensed phase with a large ensemble of particles were further conducted.

The MD simulations of the Li-ion solvation environment in pristine electrolyte show that while there is no preferential localization of the cation with respect to counterions or solvent molecules, the coordination ability of Li-ion to electrolyte constituents/additives is higher for EC molecules (coordination number, cn = 2.14) than for DEC (cn = 1.94); and FEC (cn = 0.05) has the poorest Li-ion coordination ability, as shown in Fig. 3F–H, consistent to semi-competitive solvation phenomenon in the carbonate-based electrolytes (32). Unlike PEOS, the CES can redistribute the Li-ion local coordination environment, leading to a weakening of Li coordination ability to EC and DEC (cn = 0.069). A statistical description of the Li-ion coordination ability within the solvation shell (Fig. 3I–K) shows dominant contribution of EC and DEC molecules (LiEC₂DEC₂, Fig. 3L) for all the considered systems, where the probability of such ion-molecular complex reduces from 44.5% in

contribution

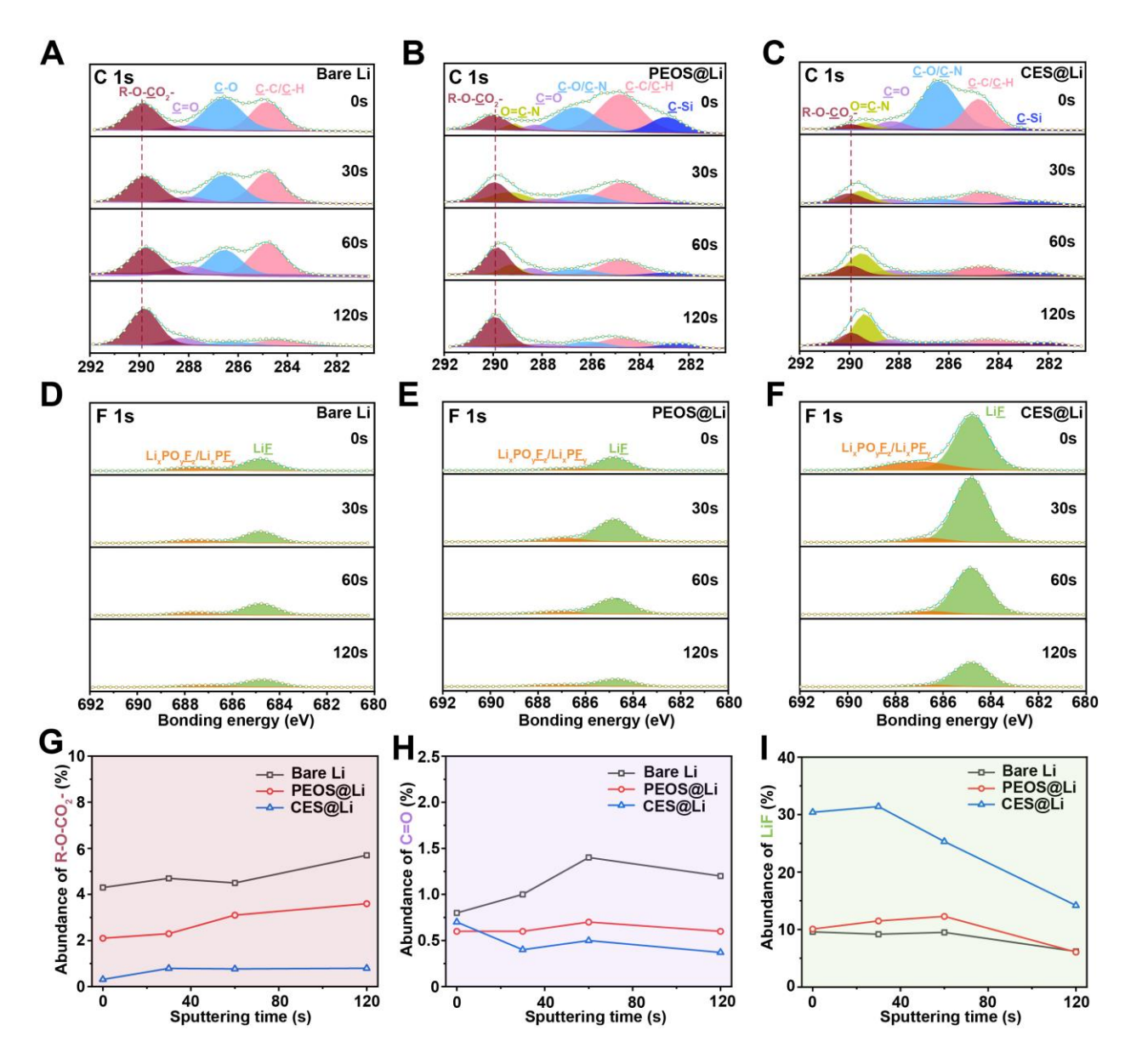


Fig. 4. The XPS depth profiling data of the formed SEI layer. (A–F) High-resolution C 1s and F 1s depth profiling XPS spectra of the formed SEI of bare Li (A and B), PEOS@Li (B and E) and CES@Li (C and F), after 10 cycles. (G–I,) Depth profiling of the absolute intensity of SEI components R-O-CO₂- (G), C=O (H) and LiF (I) for bare Li, PEOS@Li, and CES@Li.

fraction of CES in the Li-ion solvation shell of is around 16.4%, e.g., LiCES₁EC₁DEC₁ + LiCES₁EC₂, (Fig. 3M) in contrast to the negligible contribution fraction (< 3.5%) of PEOS in Li-

ion solvation shell (Fig. 3N). Together, all these NMR and theoretical modeling results corroborate the selective desolvation on EC over DEC and FEC and an enrichment of FEC in the presence of CES material.

249

250

251

252

253

254

255

256

257

258

259

260

261

262

263

264

265

266

267

268

269

270

Further studies were conducted to apply the CES coating material on Li metal with the desolvation function to alter SEI formation process and tune compositional distribution and structure of SEI on Li metal. To reveal the SEI composition aroused by the application of the CES desolvation layer, we elucidated the interfacial chemical compositions using the XPS depth profiling analysis on Li metal anodes obtained from Li||LCO pouch cells after 10 cycles. As shown in the high-resolution C 1s and F 1s XPS spectra (Fig. 4A–F). The peak intensities and relative contents of R-O-CO₂- species (at ~289.8 eV) and C=O (at ~288.2 eV), which can be only generated from the decomposition of the carbonate solvents (EC, DEC, and FEC), clearly reduce in the presence of CES coating layer (Fig. 4C), indicating the mitigated parasitic reaction between the carbonate solvent and Li metal anode. Meanwhile, the peaks at 684.8 eV in the F 1s spectra attributed to LiF show an apparent increase in peak intensities, suggesting a LiFdominant SEI formed on the Li metal anode with the CES coating layer (Fig. 4F), compared with bare Li (Fig. 4D) and PEOS-coated Li metal anode (Fig. 4E). Furthermore, the abundance depth profiles of SEI components (R-O-CO₂-, C=O species, and LiF) quantitatively verify reduced content of organic SEI components of R-O-CO₂- and C=O species and increased content of LiF SEI component in the CES coating layer than PEOS coating layer and bare Li metal (Fig. 4G–I). Echoing the ¹³C and ¹H NMR studies, the generation of an inorganic-rich SEI with LiF as the dominant species can be explained by the decreased participation of organic solvent EC and DEC in SEI formation due to the desolvation effect of the CES coating layer, along with an

enrichment of Li-ion weakly coordinating FEC in the CES coating layer, which contributes to the formation of more LiF in SEI layer (33).

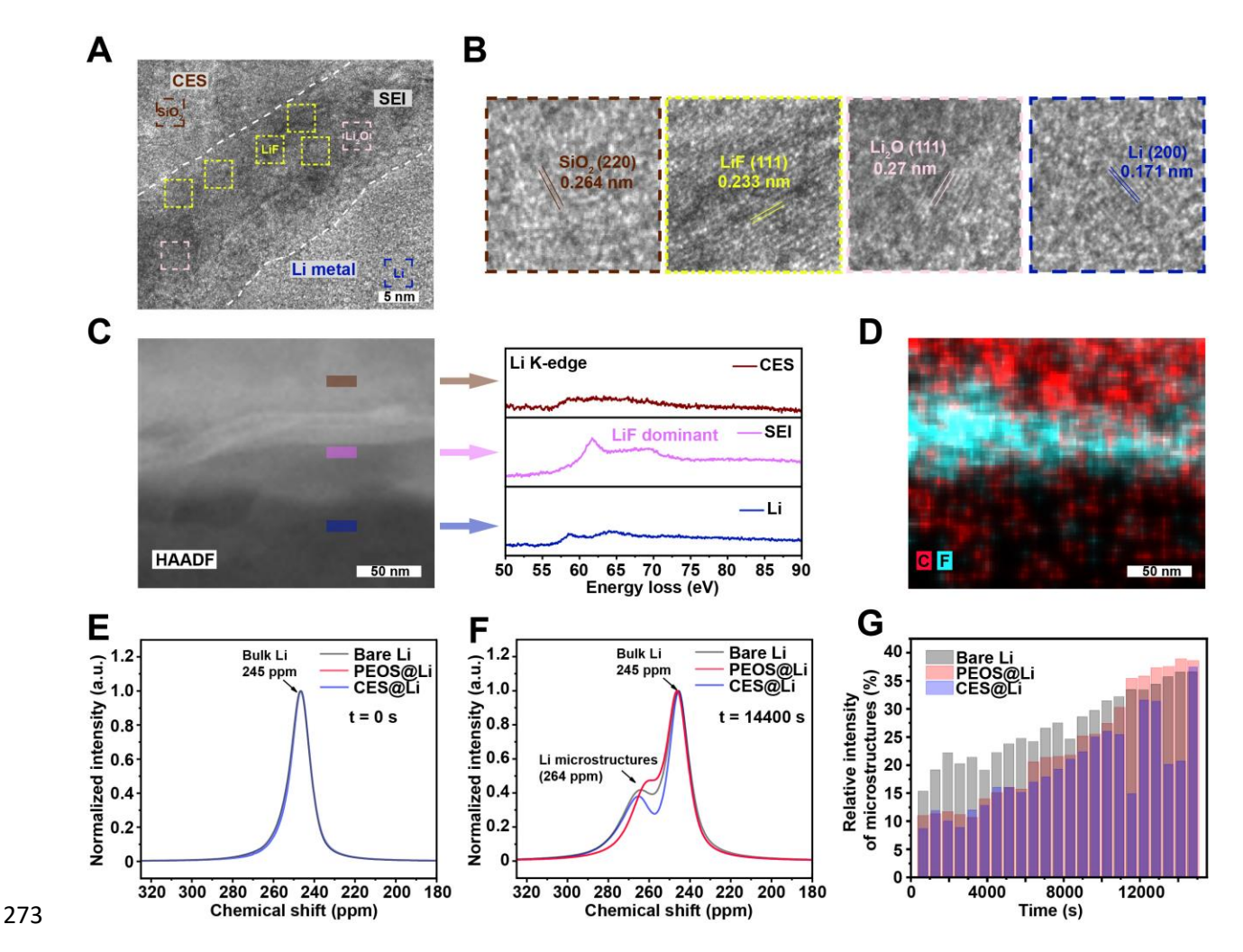


Fig. 5. The nanostructures of SEI layer and the operando ⁷**Li NMR analysis.** (**A** and **B**) The cryo-TEM images of the formed SEI facilitated by CES. (**C** and **D**) The HAADF-STEM image and the corresponding Li K-edge spectra (**C**) and EDS mapping of elements C, F(**D**). (**E**–**G**) Operando ⁷Li NMR spectroscopy results of symmetric Li||Li cells with and without coating. ⁷Li NMR spectra taken prior to plating (**E**) and after 4 h (14400 s) of Li metal plating at a current density of 1 mA/cm² (**F**). Areal intensities of the Li microstructures (⁷Li NMR chemical shifts >245 ppm) relative to bulk metallic Li (chemical shift of 245 ppm) during plating (**G**).

The formed SEIs with and without the CES coating layer are further investigated using cryo-TEM techniques, showing significant differences in both nanostructures and dominant species. Fig. 5A shows a high-resolution cryo-TEM image of SEI on CES-coated Li metal, displaying three-layer structures from top to bottom with different contrasts assigned to the CES coating layer, SEI, and the deposited Li metal. The formed SEI is dense, uniform, and thin (thickness around 14 nm). In the CES coating layer, a lattice spacing of 0.264 nm (Fig. 5A and 5B, the squared region in maroon) confirmed by the Fast Fourier Transform (FFT) technique (SI Appendix, Fig. S35) matches well with the {220} SiO₂ plane. In the SEI, the {111} LiF plane with a lattice spacing of 0.233 nm (Fig. 5A and 5B, the squared region in yellow) and the {200} Li plane with a lattice spacing of 0.171 nm (Fig. 5A and 5B, the squared region in blush) were observed and confirmed by the FFT technique (SI Appendix, Fig. S35). Accordingly, the LiF species is dominant in the formed SEI, which is consistent with SEI composition illustrated in XPS depth profiling. The inorganic LiF dominant SEI composition improves robustness of the SEI, facilitates uniform Li deposition, and suppresses Li dendrite growth (34). In contrast, the formed SEI on the bare Li metal anode is much thicker (thickness around 20 nm) and shows a laminar Li₂O as the thin outer layer along with an amorphous phase dominant inner layer (SI Appendix, Fig. S37 and S38), similar to previously reported results (35).

The LiF-dominant SEI on the CES-coated Li metal was further verified by electron energy loss spectroscopy (EELS) and energy dispersive X-ray spectroscopy (EDS) studies. As shown in Fig. 5C, a high-angle annular dark-field scanning transmission electron microscopy (HAADF-STEM) image was obtained for the formed SEI with the CES coating layer. Three selected regions representing the CES coating layer (in maroon), SEI (in pink), and the deposited Li layer (in blue) were analyzed pixel by pixel. The Li K-edge spectrum obtained from the top maroon area shows low Li intensity, as indicative of the CES coating layer. In the middle pink area for SEI, the peak shape corresponds to LiF, suggesting the formation of a LiF-dominant SEI. The spectrum taken from the bottom blue area corresponds to the metallic Li. Based on the HAADF-

STEM image, the EDS elemental mapping image of C and F was collected, as shown in Fig. 5D. The top layer containing a strong C signal corresponds to the CES coating layer. The middle SEI shows a very weak C signal but evidently strong F signal, suggesting much reduced organic solvent decomposition during the SEI formation process, and a robust F-dominant SEI layer with greatly reduced organic species, when using the CES desolvation coating layer. The bottom layer with very weak C, and F signals was assigned to the metallic Li. In contrast, in the EDS elemental mapping image of C and F for a bare Li metal anode, the formed SEI shows a very weak F signal and a clearly strong C signal, indicating an organic-rich SEI formed (SI Appendix, Fig. S37D). Overall, these microscopic characterization results are consistent with the XPS depth profiling analysis, and further verify the generation of a LiF-dominant SEI with greatly reduced organic species due to the selective desolvation of the strongly Li-ion coordinating EC and the enrichment of the weakly Li-ion coordinating FEC by the CES coating layer, resulting in suppressed carbonate decomposition during the SEI formation.

Furthermore, operando ⁷Li solid-state NMR spectroscopy was employed to evaluate the impact of the PEOS and CES coatings on the resulting microstructures of the deposited Li (Fig. 5*E*–*G* and *SI Appendix*, Fig. S40). The NMR spectra were acquired by plating 4 mAh/cm² Li under a current density of 1 mA/cm². The chemical shift of Li correlates with the roughness of Li microstructures and, as a general trend, the rougher the surface, the higher the observable chemical shift (36, 37). The chemical shift of bulk Li metal typically ranges between 245 ppm and 247 ppm, whereas signals reflecting more inhomogeneous Li microstructures, such as mossy and dendritic deposits, have chemical shifts between 250 ppm and 280 ppm (38, 39). As demonstrated in Fig. 5*E* and 5*F*, compared to bulk Li, a shoulder-like peak forms after plating for 4 h (14400 s) that can be assigned to Li microstructures. All ⁷Li NMR spectra were fitted

with a custom-made MATLAB script, detailed representative fits are included in the Methods section. Based on chemical shifts of 260 ppm and 264 ppm in the case of bare and coated Li metal electrodes, respectively, the microstructures are mostly comparable to mossy-type Li deposits. The slightly higher chemical shift of PEOS and CES-coated Li metal could be attributed to interfacial reactions that roughen/affect the Li surface to a larger extent compared to the bare Li. The development of the shoulder related to Li microstructure over time is shown in Fig. 5G. Note that the intensity (integrated peak area) of the shoulder peaks is reported relative to the total Li metal signal intensity (microstructure + bulk metal). Bare Li metal electrodes accumulate comparably large amounts of microstructural deposits starting from 15 % during the initial phase until ca. 36 % after 14400 s (4 h) of plating, whereas the coated electrodes exhibit lower ratios of microstructural deposits, with CES having the lowest amount throughout the whole time of the experiment. After about 10000 s (2.8 h), the ratio of microstructures for PEOScoated Li is close to that of the bare Li, indicating that the limit may be reached (corresponding to 2.8 mAh/cm²). Moreover, the SEM studies of the cycled Li metal anodes morphologies consistently reveal that the CES coating layer promotes a much uniform surface with the least mossy Li formation, compared with the bare and PEOS-coated Li metal anodes (SI Appendix, Fig. S28), suggesting the superiority of CES to facilitate uniform Li deposition.

347

330

331

332

333

334

335

336

337

338

339

340

341

342

343

344

345

346

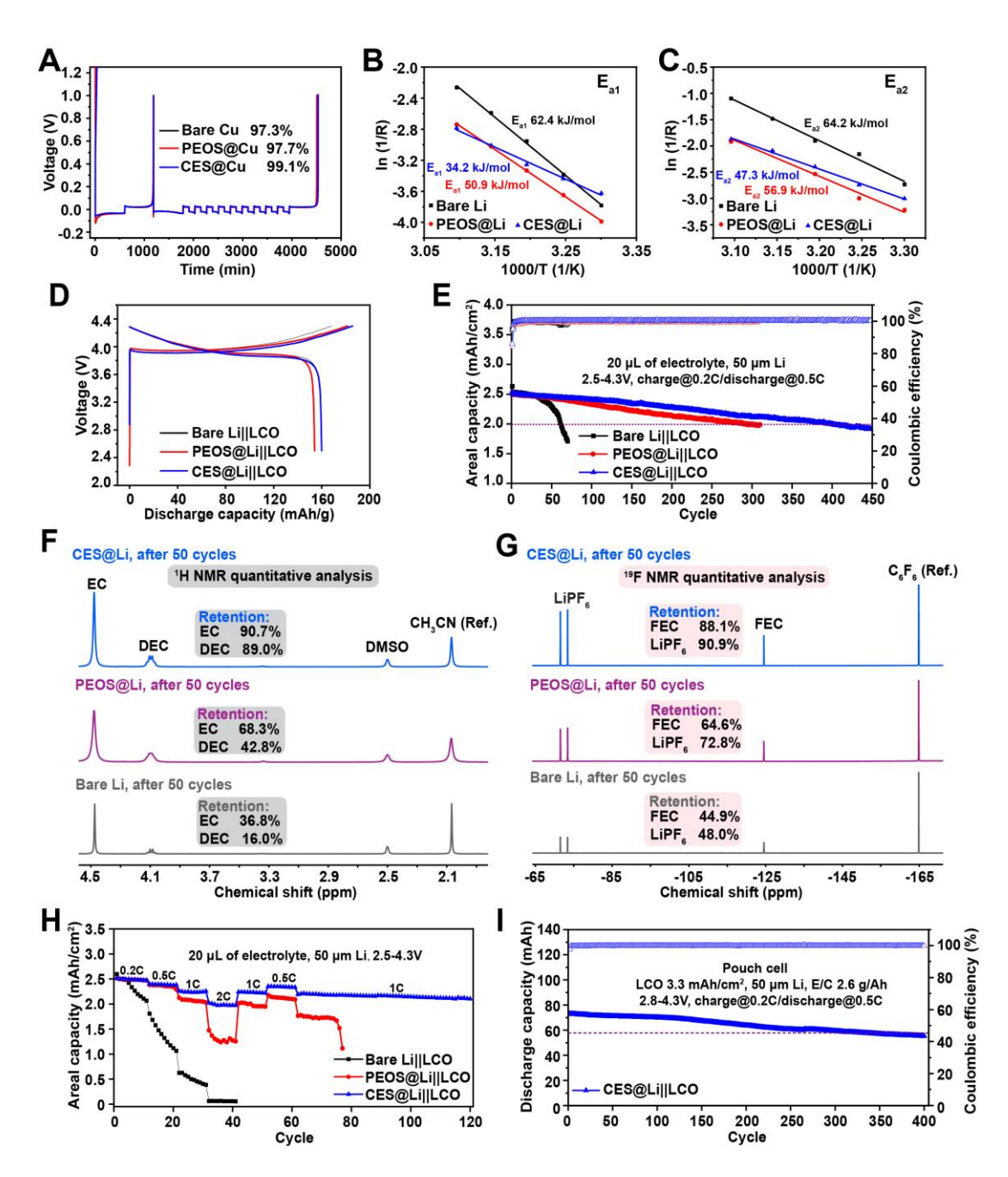


Fig. 6. Electrochemical performance and the NMR spectroscopic analysis on electrolyte evolution. (A) CE measurement of Li plating/striping in Li||Cu cells. (**B** and **C**) Arrhenius behavior and comparison of the activation energies in Li||Li symmetric cells with/without coating. E_{a1} represents the activation energy in the transport of Li-ion in SEI layer (**B**), and E_{a2} represents the activation energy in the desolvation process of Li-ion (**C**). (**D**) Voltage profiles of Li (50 μm) ||LCO full cells for the pre-cycling cycles at 0.1 C, 2.5–4.3 V. (**E**) Electrochemical performance of Li (50 μm) ||LCO full cells between 2.5–4.3 V, charging@0.2C and discharging@0.5C. (**F**) The 1 H quantitative NMR spectroscopic analysis of carbonate solvents (EC and DEC) in Li (50 μm) ||LCO full cells after 50 cycles, acetonitrile (CH₃CN) was used as the internal reference. DMSO: dimethyl sulfoxide. (**G**) The 19 F quantitative NMR spectroscopic analysis of F-containing species (FEC and LiPF₆) in Li||LCO full cells after 50 cycles, hexafluorobenzene (C_6 F₆) was used as the internal reference. (**H**) Electrochemical performance of Li (50 μm) ||LCO full cells between 2.5–4.3 V at different C rates. 20 μL of 1 M LiPF₆ in EC/DEC (v/v = 1:1) with 15 wt% FEC was used for each case. 1C = 2.5 mA/cm². (**I**) Electrochemical performance of Li (50 μm) ||LCO pouch cell between 2.8–4.3 V, 2.6 g/Ah of 1 M LiPF₆ in EC/DEC (v/v = 1:1) with 15 wt% FEC was used. 1C = 3.3 mA/cm².

Encouraged by the results above, we next evaluated the electrochemical behaviors of Li metal anodes with/without the coating layer. Firstly, the Li||Cu half cells were utilized to evaluate the Li plating/striping CE (40) in the conventional mixed carbonate electrolyte (1 M LiPF₆ in EC/DEC (v/v = 1:1) with 15 wt% FEC). As shown in Fig. 6A, an apparently improved CE of 99.1% was achieved in the presence of the CES-coated Cu, compared to a CE of 97.3% for bare Cu and a slightly improved CE of 97.7% for the PEOS-coated Cu, under a current density of 0.5 mA/cm² and Li deposition capacity of 1.0 mAh/cm². Furthermore, the Li||Cu half-cell using CES-coated Cu delivered improved and stable CEs over 400 cycles. In contrast, the bare Cu and PEOS-coated Cu showed a rapid drop after only 130 and 215 cycles, respectively (SI Appendix, Fig. S41). To evaluate the kinetics of Li-ion transfer with/without the coating layer on the Li metal anode surface, the temperature dependent electrochemical impedance spectroscopy (EIS) studies of Li||Li symmetric cells were conducted to calculate the activation energies of the Li-ion transport processes (SI Appendix, Fig. S42). As shown in Fig. 6B and 6C, both the activation energy E_{a1} corresponding to the transport process of Li-ion in SEI layer and the E_{a2} corresponding to the desolvation energy of Li-ion are in line with the law of Arrhenius (41). The Li||Li cell with CES coating exhibits a significantly lower activation energy, E_{a1} (34.2 kJ/mol), compared to bare Li (62.4 kJ/mol) and PEOS coating (50.9 kJ/mol). More importantly, the CES coating shows a noticeably lower activation energy, E_{a2} (47.3 kJ/mol), compared to bare Li (64.2 kJ/mol) and PEOS coating (56.9 kJ/mol), confirming the effectiveness of CES coating to facilitate the desolvation process of Li-ion. The revealed smaller E_{a1} and E_{a2} enabled by CES coating verified the enhanced kinetics of Li-ion transfer both in the SEI layer and the desolvation process.

363

364

365

366

367

368

369

370

371

372

373

374

375

376

377

378

379

380

381

382

383

The Li||LCO full cells were next assembled with 50 µm thin Li anodes and LCO cathode of 2.5 mAh/cm² areal capacity using the conventional mixed carbonate electrolyte, and electrochemically tested between 2.5–4.3 V. After pre-cycling at 0.1C for one cycle, the Li||LCO full cells were then cycled at 0.2 C for charge and 0.5 C for discharge. All cells exhibited similar charge/discharge voltage profiles during pre-cycling and delivered comparable dischargespecific capacities of approximately 160 mAh/g (Fig. 6D). As shown in Fig. 6E, the cell with bare Li metal anode decays fast and reaches 80% of capacity retention only after 62 cycles. With PEOS-coated Li metal anode, the cell shows an improved cycling performance, reaching 80% of capacity retention after 293 cycles. In contrast, the cell with CES-coated Li metal anode demonstrates significantly improved cycling performance, delivering an 80% capacity retention after 404 cycles. The efficacy of CES coating was further confirmed through parallel cells (SI Appendix, Fig. S51). The ¹H quantitative NMR spectroscopic analysis was conducted to study the carbonate solvent evolution upon cycling in Li||LCO full cells. After 50 cycles, excellent retentions of EC (90.7%) and DEC (89.0%) were achieved with the CES-coated Li metal anode (Fig. 6F), in contrast to the considerable consumption of EC and DEC with bare Li (36.8% retention of EC and 16.0% retention of DEC) and PEOS-coated Li metal anode (68.3% retention of EC and 42.8% retention of DEC). The ¹⁹F quantitative NMR spectroscopic analysis disclosed the evolution of F-containing species (FEC and LiPF₆). As shown in Fig. 6G, the CES coating layer also significantly delays the consumption of FEC (88.1% retention) and LiPF₆ (90.9% retention). The above quantitative NMR results evidently reveal the retarded consumption of carbonate solvents (EC and DEC) and F-containing compounds (FEC and LiPF₆) in the presence of CES-coated Li, illustrating the suppressed electrolyte decomposition via the selective Li-ion desolvation layer. The rate performance of the Li||LCO full cells is further tested (Fig. 6H). The

385

386

387

388

389

390

391

392

393

394

395

396

397

398

399

400

401

402

403

404

405

406

cell incorporating the CES-coated Li metal anode delivers stable cyclability at all C rates (0.2 C, 0.5 C, 1C and 2C) along with the higher capacities, compared with bare Li and PEOS-coated Li metal anode. Furthermore, a Li||LCO pouch cell using CES-coated Li metal anode was assembled and tested under practical conditions, with a high areal capacity (3.3 mAh/cm²) of LCO cathode, 50 μ m thin Li metal anode (N/P ratio of 3.0) and lean electrolyte (E/C ratio of 2.6 g/Ah). The pouch cell can deliver a high gravimetric energy density of 312 Wh/kg (based on cathode electrode, Li metal electrode, separator, electrolyte and the applied CES coating material, *SI Appendix*, Table S1), and demonstrated an unprecedented cycling performance with an 80% capacity retention after 333 cycles using the conventional mixed carbonate electrolyte of 1 M LiPF₆ in EC/DEC (y/v = 1:1) with 15 wt% FEC (Fig. 6*I*).

Conclusions

In summary, this study presents a novel strategy employing a desolvation coating layer containing 12-C-4 ether structural moieties to actively modulate the Li-ion solvation structure at the interface and thereby influence organic solvent participation in SEI formation. This approach offers a distinct pathway for altering the desolvation process in SEI formation by actively controlling the organic components, distinguishing it from widely reported approaches focused on promoting inorganic component generation. Experimental investigations in a Li metal incompatible carbonate electrolyte revealed that the desolvation coating layer selectively displaces strongly coordinating solvent, enriching weakly coordinating fluorinated solvents at the Li metal/electrolyte interface. This selective desolvation and enrichment result in the formation of a LiF-dominant SEI with greatly reduced organic species on the Li metal surface, as confirmed by XPS, NMR, cryo-TEM, EELS, and EDS characterizations. By tailoring the desolvation functionality, this study demonstrates the ability to manipulate the composition and

- 431 structure of SEI layer on Li metal, leading to excellent rate performance and long cycling life of
- 432 Li metal batteries in practical conditions.

434

References

- 1. J. Liu et al., Pathways for practical high-energy long-cycling lithium metal batteries. Nat.
- 436 Energy **4**, 180 (2019).
- 2. D. Lin, Y. Liu, Y. Cui, Reviving the lithium metal anode for high-energy batteries. *Nat.*
- 438 *Nanotechnol.* **12**, 194 (2017).
- 439 3. P. Albertus, S. Babinec, S. Lizelman, A. Newman, Status and challenges in enabling the
- lithium metal electrode for high-energy and low-cost rechargeable batteries. *Nat. Energy* **3**,
- 441 16 (2018).
- 442 4. S. Jiao *et al.*, Stable cycling of high-voltage lithium metal batteries in ether electrolytes. *Nat.*
- 443 Energy 3, 739 (2018).
- 5. R. Weber *et al.*, Long cycle life and dendrite-free lithium morphology in anode-free lithium
- pouch cells enabled by a dual-salt liquid electrolyte. *Nat. Energy* **4**, 683 (2019).
- 446 6. X. Ren et al., Role of inner solvation sheath within salt–solvent complexes in tailoring
- electrode/electrolyte interphases for lithium metal batteries. *Proc. Natl. Acad. Sci. U.S.A.*
- **117**, 28603 (2020).

- 449 7. X. Cao et al., Effects of fluorinated solvents on electrolyte solvation structures and
- electrode/electrolyte interphases for lithium metal batteries. *Proc. Natl. Acad. Sci. U.S.A.*
- **118**, e2020357118 (2021).
- 8. G. M. Hobold et al., Moving beyond 99.9% Coulombic efficiency for lithium anodes in
- liquid electrolytes. *Nat. Energy* **6**, 951 (2021).
- 454 9. W. Xue et al., Ultra-high-voltage Ni-rich layered cathodes in practical Li metal batteries
- enabled by a sulfonamide-based electrolyte. *Nat. Energy* **6**, 495 (2021).
- 456 10. Z. Yu et al., Rational solvent molecule tuning for high-performance lithium metal battery
- 457 electrolytes. *Nat. Energy* **7**, 94 (2022).
- 458 11. Y. Gao et al., Polymer-inorganic solid-electrolyte interphase for stable lithium metal
- batteries under lean electrolyte conditions. *Nat. Mater.* **18**, 384 (2019).
- 460 12. Z. Yu et al., A dynamic, electrolyte-blocking, and single ion-conductive network for stable
- 461 lithium metal anodes. *Joule* **3**, 2761 (2019).
- 462 13. Y. Gao *et al.*, Low-temperature and high-rate-charging lithium metal batteries enabled by an
- electrochemically active monolayer-regulated interface. *Nat. Energy* **5**, 534 (2020).
- 464 14. S. Li et al., A robust all-organic protective layer towards ultrahigh-rate and large-capacity Li
- 465 metal anodes. *Nat. Nanotechnol.* **17**, 613 (2022).
- 466 15. J. Lopez *et al.*, Effects of polymer coatings on electrodeposited lithium metal. *J. Am. Chem.*
- 467 *Soc.* **140**, 11735 (2018).
- 16. H. Zhou, S. Yu, H. Liu, P. Liu, Protective coatings for lithium metal anodes: Recent progress
- and future perspectives. *J. Power Sources* **450**, 227632 (2020).

- 470 17. J. Li et al., Polymers in lithium-ion and lithium metal batteries. Adv. Energy Mater. 11,
- 471 2003239 (2021).
- 472 18. N. von Aspern, G.-V. Roschenthaler, M. Winer, I. Cekic-Laskovic, Fluorine and lithium:
- ideal partners for high-performance rechargeable battery electrolytes. *Angew. Chem. Int. Ed.*
- **58**, 15978 (2019).
- 475 19. M. S. Kim *et al.*, Suspension electrolyte with modified Li⁺ solvation environment for lithium
- 476 metal batteries. *Nat. Mater.* **21**, 445 (2022).
- 477 20. X. Cao et al., Monolithic solid–electrolyte interphases formed in fluorinated orthoformate-
- based electrolytes minimize Li depletion and pulverization. *Nat. Energy* **4**, 796 (2019).
- 479 21. H. Wu, H. Jia, C. Wang, J.-G. Zhang, W. Xu, Recent progress in understanding solid
- electrolyte interphase on lithium metal anodes. *Adv. Energy Mater.* **11**, 2003092 (2021).
- 481 22. X. He *et al.*, The passivity of lithium electrodes in liquid electrolytes for secondary batteries.
- 482 *Nat. Rev. Mater.* **6**, 1036 (2021).
- 483 23. B. Horstmann et al., Strategies towards enabling lithium metal in batteries: interphases and
- 484 electrodes. *Energy Environ. Sci.* **14**, 5289 (2021).
- 485 24. K. Xu, Electrolytes and interphases in Li-ion batteries and beyond. *Chem. Rev.* **114**, 11503
- 486 (2014).
- 487 25. T. Li *et al.*, Fluorinated solid-electrolyte interphase in high-voltage lithium metal batteries.
- 488 *Joule* **3**, 2647 (2019).
- 489 26. Z. Shadike *et al.*, Engineering and characterization of interphases for lithium metal anodes.
- 490 *Chem. Sci.* **13**, 1547 (2022).

- 491 27. L. Sheng *et al.*, Suppressing electrolyte-lithium metal reactivity via Li⁺-desolvation in
- uniform nano-porous separator. *Nat. Commun.* **13**, 172 (2022).
- 493 28. J. Henine et al., Fluoroethylene carbonate as electrolyte additive in tetraethylene glycol
- dimethyl ether based electrolytes for application in lithium ion and lithium metal batteries. J.
- 495 *Electrochem. Soc.* **162**, A1094 (2015).
- 496 29. G. Li *et al.*, Stable metal battery anodes enabled by polyethylenimine sponge hosts by way of
- 497 electrokinetic effects. *Nat. Energy* **3**, 1076 (2018).
- 498 30. Z. Xue, D. He, X. Xie, Poly(ethylene oxide)-based electrolytes for lithium ion batteries. J.
- 499 *Mater. Chem. A* **3**, 19218 (2015).
- 31. P. Growth, On the crystal structure of the (1:1) complex between lithium thiocyanate and
- 501 1,4,7,10-tetraoxacyclododecane at room temperature. *Acta. Chem. Scand.* **35a**, 463 (1981).
- 502 32. A. J. Ringsby et al., Transport phenomena in low temperature lithium-ion battery
- electrolytes. *J. Electrochem. Soc.* **168**, 080501 (2021).
- 33. Z. Zhu *et al.*, Fluoroethylene carbonate enabling a robust LiF-rich solid electrolyte interphase
- to enhance the stability of the MoS₂ anode for lithium-ion storage. Angew. Chem. Int. Ed. 57,
- 506 3656 (2018).
- 34. Y. Lu, Z. Tu, L. A. Archer, Stable lithium electrodeposition in liquid and nanoporous solid
- 508 electrolytes. *Nat. Mater.* **13**, 961 (2014).
- 509 35. Y. Xu et al., Atomic to nanoscale origin of vinylene carbonate enhanced cycling stability of
- lithium metal anode revealed by cryo-transmission electron microscopy. *Nano Lett.* **20**, 418
- 511 (2020).

- 36. H. J. Chang et al., Investigating Li microstructure formation on Li anodes for lithium
- batteries by in Situ ⁶Li/⁷Li NMR and SEM. *J. Phys. Chem. C* **119**, 16443 (2015).
- 37. V. Kupers et al., In situ ⁷Li-NMR analysis of lithium metal surface deposits with varying
- electrolyte compositions and concentrations. *Phys. Chem. Chem. Phys.* **21**, 26084 (2019).
- 516 38. Y.-C. Hsieh et al., Quantification of dead lithium via in situ nuclear magnetic resonance
- 517 spectroscopy. *Cell Rep. Phys. Sci.* **1**, 100139 (2020).
- 39. Y.-C. Hsieh et al., Revealing the impact of film-forming electrolyte additives on lithium
- metal batteries via solid-state NMR/MRI analysis. *J. Phys. Chem. C* **125**, 252 (2021).
- 520 40. B. D. Adams, J. Zheng, X. Ren, W. Xu, J.-G. Zhang, Effects of carbonate solvents and
- lithium salts on morphology and Coulombic efficiency of lithium electrode. Adv. Energy
- 522 *Mater.* **8**, 1702097 (2018).
- 523 41. C. Yan et al., Regulating the inner Helmholtz plane for stable solid electrolyte interphase on
- 524 lithium metal anodes. *J. Am. Chem. Soc.* **141**, 9422 (2019).

Materials and Methods

526 Materials

- 527 The LCO cathode electrode was purchased from Guangdong Canrd New Energy Technology
- 528 Co.,Ltd. with the active material loading of ~16.0 mg/cm² (discharge capacity: ~160
- mAh/g@0.1C, 2.5-4.3 V) and punched into small discs with an electrode area of 0.785 cm² for
- 530 the Li||LCO coin cells assembly. Battery-grade LiPF₆, FEC, EC, DEC and ethyl methyl
- 531 carbonate (EMC) were purchased from Gotion. PEI (branched, average M_n ~10000), PEO
- (average M_v ~1000000) and 12-crown-4 (98%) were purchased from Sigma-Aldrich and used as
- received without further purification. Li chips with the thickness of 600 µm for Li||Cu half cells,

and Li foil with the thickness of 50 μ m bonded to Cu substrate (~5 μ m) were purchased from China Energy and used as received without further treatment. The Cu foil with the thickness of 9 μ m for Li||Cu half cells was purchased from MTI. Celgard 2325 with the thickness of 25 μ m was used as separators for all cells. Electrolyte (1 M LiPF₆ in EC/DEC (v/v = 1:1) with 15 wt % FEC) was prepared inside an Ar-filled glovebox (O₂ <0.1ppm, H₂O <0.1ppm) and used freshly. All other reagents and solvents were purchased from Sigma-Aldrich and used without further purification unless otherwise stated.

Electrochemical testing

Electrochemical testing of cells was carried out on Landt battery testers using CR2016 coin cells under galvanostatic charging/discharging conditions. The Li||Cu half cells cycling CE testing was carried out by depositing 1 mAh/cm² of Li onto the Cu electrode followed by stripping to 1.0 V, under a current density of 0.5 mA/cm^2 with $50 \mu\text{L}$ of electrolytes. For the CE testing, a standard protocol was followed: 1) run one initial formation cycle with Li deposition capacity of 5 mAh/cm^2 on Cu substrate under a current density of 0.5 mA/cm^2 and then strip to 1.0 V; 2) deposit 5 mAh/cm^2 of Li as a Li reservoir onto Cu substrate under 0.5 mA/cm^2 ; 3) repeatedly strip/deposit Li of 1 mAh/cm² under 0.5 mA/cm^2 for 9 cycles; 4) strip all the Li metal to 1.0 V. All of the Li||LCO coin cells were assembled with $50 \mu\text{m}$ Li anodes and $20 \mu\text{L}$ of 1 M LiPF₆ in EC/DEC (v/v = 1:1) with 15 wt % FEC as electrolyte. After one formation cycle at 0.1 C for charge/discharge, the coin cells were cycled at 0.2 C for charge and 0.5 C for discharge between 2.5–4.3 V. For the rate performance evaluation, after one formation cycle at 0.1 C for charge/discharge, the Li||LCO coin cells were then cycled at the corresponding C-rates (0.2 C, 0.5 C, 1 C and 2 C) for charge/discharge between 2.5–4.3 V.

Characterizations

SEM images were captured on Nova NanoSEM 630 instrument. XPS experiments were carried out on PHI VersaProbe II Scanning XPS Microprobe. The air and moisture sensitive samples were loaded in a glovebox and transferred into the instrument through a vacuum transfer vessel. For the XPS measurements, the Li metal anode obtained by disassembling the Li||LCO pouch cells after 10 cycles (pre-cycling at 0.1C for one cycle, the cells were then cycled for 10 cycles with a charge rate of 0.2C and a discharge rate of 0.5C) were washed with EMC for 3 times to remove the electrolyte residues on surface. ¹H, ¹³C and ¹⁹F NMR spectra were carried out on Bruker AVANCE NEO-400 instruments. The coaxial set (Wilmad® coaxial insert, complete set, inner tube O.D. \times I.D. 2.52 mm \times 1.5 mm) was used for the ¹³C NMR studies on the solvation structure of electrolytes to eliminate the potential influence on solvation structure aroused by deuterated solvents, the peaks observed in the recorded ¹³C spectra are referenced relative to the internal standard (DMSO, $\delta = 39.40$ ppm) loaded in inner tube of the coaxial insert. Acetonitrile was used as the internal reference for the ¹H quantitative analysis of electrolyte evolution after 50 cycles. Hexafluorobenzene was used as the internal reference for the ¹⁹F quantitative analysis of electrolyte evolution after 50 cycles. For every single Li||LCO coin cell, 20 µL of 1 M LiPF₆ in EC/DEC (v/v = 1:1) with 15 wt % FEC was used. After 50 cycles, the corresponding coin cells were disassembled and carefully rinsed with DMSO- d_6 (~2 mL). To the collected solution, 3.0 µL of acetonitrile and 2.0 µL of hexafluorobenzene were added as internal references. The EIS measurements of the Li||Cu half cells were carried out on Solartron ModuLab in the frequency range of 1 MHz to 0.01 Hz with an amplitude of 10 mV. Operando ⁷Li NMR spectroscopy was performed at a Bruker Avance III 200 MHz (4.7 T) spectrometer equipped with a custom-made broadband (¹H, ¹⁹F//(X= ⁶Li - ⁷Li) probe. Symmetric

Li||Li pouch type cells (electrode thickness 300 µm, area 1.25 cm²) were polarized at 20 °C with

557

558

559

560

561

562

563

564

565

566

567

568

569

570

571

572

573

574

575

576

577

578

a current density of 1 mA/cm² for 4 h (4 mAh/cm²). The spectrometer was operated at resonance frequency of 77.8 MHz, the pulse length of the rf pulse was set to 16 μs at a power of 80 W. Calibration of the reference shift (0 ppm) was carried out with a 1 M LiCl + 0.1 g/L CuSO₄ standard solution in a pouch type cell. For signal averaging, a relaxation delay of 1 s was optimized for the peak assigned to bulk Li metal at around 246 ppm. Note that the corresponding ⁷Li NMR peaks of the electrolyte and SEI compounds were in the range of –20 and 20 ppm and therefore not considered in the optimization range. Data processing and fitting was performed using Bruker Topspin software and a custom-made MATLAB script, respectively.

Cryo-TEM experiment

The bare Li sample without coating was prepared by depositing Li on bare Cu grid, with a deposition capacity of 0.25 mAh/cm² under a current density of 0.5 mA/cm². The obtained bare Li sample on Cu grid was washed with EMC and dried in vacuum for 10 minutes. Afterwards, the obtained bare Li metal sample was immediately transferred to the cryo-TEM holder for characterization to minimize its exposure to air. The CES-coated Li sample for cross-sectional TEM was prepared on an FEI Helios Nanolab 660 Dual Beam focused ion beam using the 'in situ lift-out' technique. A thin section was extracted from the cycled CES-coated Li metal anode and then attached to a TEM grid using an initial ion beam voltage of 30 kV. The resultant sample underwent a thinning process using lower ion beam voltages in a successive manner. Starting from the initial voltage, the voltage was gradually reduced until it reached 2 kV, resulting in a final thickness of approximately 100 nm. Afterwards, the obtained sample for CES-coated Li was immediately transferred to the cryo-TEM holder for characterization to minimize its exposure to air. TEM and STEM images were then acquired using a dual spherical aberration-corrected FEI Titan 2G 2 60-300 STEM operating at an accelerating voltage of 200 kV. The EDS

maps were acquired in STEM mode using Bruker Super-X quad X-ray detectors, which, when coupled with a high-brightness X-field emission gun source, were able to produce high-quality elemental maps within 5 minutes at a beam current of around 0.1 nA. EELS spectral imaging was carried out using a Gatan GIF Quantum ERS 966 system. The EELS data was collected with an exposure time of 0.1 s and a dispersion of 0.05 eV per channel, while maintaining a pixel size of 10 nm.

Fabrication and electrochemical testing of the pouch cell

For the double layer pouch cell, one piece of double-side coated LCO electrode (active material mass loading: ~21.0 mg/cm² for every single side, purchased from Guangdong Canrd New Energy Technology Co.,Ltd.) with area of 11.31 cm² (length: 3.9 cm, width: 2.9 cm), two pieces of Li foil (thickness: $50 \mu m$, area of $12.0 cm^2$, length: 4.0 cm, width: 3.0 cm) one-side laminated onto Cu substrate (thickness: $\sim 5 \mu m$) and two pieces of Celgard 2325 (thickness: $25 \mu m$) with area of $12.0 cm^2$ (length: 4.0 cm, width: 3.0 cm) were stacked together. 194 cm of 1 cm LiPF₆ in EC/DEC (v/v = 1:1) with 15 cm with 15 cm sadded as electrolyte (E/C ratio: 2.6 cm). The pouch cell was evaluated under constant-current—constant-voltage conditions. After cycling one formation cycle at 0.1 cm for charge/discharge, then the pouch cell was charged to 4.3 cm at 0.2 cm and held at 4.3 cm until the anodic current dropped below C/20 before discharged to 2.8 cm at 0.5 cm.

Computation details

All the DFT calculations were conducted in gas phase using B3LYP/6-31G(2df, p) level of theory under Gaussian code, v16. Electrostatic potential map was generated using MultiWFN, v3.8 (42). Binding energy of the considered ion-molecular complexes was accounted with basis set superposition error. All MD simulations were carried out based on OPLS/AA force field database (43, 44) from GROMACS, v2016.3. Equations of motion were integrated using leap-

- 626 frog algorithm with a time-step of 1 fs. The time-step selection was justified by utilization of
- 627 C-H bonds constrains, which was achieved with LINCS algorithm (45). The electrostatic
- 628 interactions within the cut-off range of 1.4 nm were accounted by the Particle Mesh Ewald
- algorithm (46), using the same cut-off distance for the real-space component. The 12-6 Lennard-
- Jones interactions were treated by the shifted force technique with a switch region between 1.2
- 631 and 1.3 nm.

References

- 633 42. T. Lu, F. Chen, Multiwfn: a multifunctional wavefunction analyzer. J. Comput. Chem. 33,
- 634 580 (2012).
- 635 43. W. L. Jorgensen, J. Tirado-Rives, The OPLS potential functions for proteins. Energy
- minimizations for crystals of cyclic peptides and crambin. J. Am. Chem. Soc. 110, 1657
- 637 (1988).
- 638 44. W. L. Jorgenssen, D. S. Maxwell, J. Tirado-Rives, Development and testing of the OPLS all-
- atom force field on conformational energetics and properties of organic liquids. J. Am. Chem.
- 640 *Soc.* **118**, 11225 (1996).
- 45. B. Hesss et al., LINCS: a linear constraint solver for molecular simulations. J. Comput.
- 642 *Chem.* **18**, 1463 (1997).
- 643 46. T. Darden *et al.*, Particle mesh Ewald: an $N \log(N)$ method for Ewald sums in large systems.
- 644 J. Chem. Phys. 98, 10089 (1993).
- Data, Materials, and Software Availability.
- All study data are included in the article and SI Appendix.

Acknowledgments

This work was supported by the by the Assistant Secretary for Energy Efficiency and Renewable Energy, Office of Vehicle Technologies of the US Department of Energy, through US-Germany Collaboration Projects and Argonne National Laboratory subcontracting award no. 0F-60008. We gratefully acknowledge the computing resources provided on Bebop, a high-performance computing cluster operated by the Laboratory Computing Resource Center at Argonne National Laboratory.



